coatings

MDPI

Article

High-Performance SAW-Based Microfluidic Actuators Composed of Sputtered Al–Cu IDT Electrodes

Hwansun Kim [1], Youngjin Lee [2], Peddathimula Puneetha [3], Sung Jin An [4], Jae-Cheol Park [5,*] and Siva Pratap Reddy Mallem [6,*]

1 Micro Electro Mechanical System (MEMS) Corp., Gwangju 61012, Republic of Korea; hwan@koreamems.com
2 Display Materials Center, Korea Institute of Ceramic Engineering & Technology (KICET), Jinju 52851, Republic of Korea; yjlee@kicet.re.kr
3 Department of Robotics and Intelligent Machine Engineering, College of Mechanical and IT Engineering, Yeungnam University, Gyeongsan 38541, Republic of Korea; puneethaphd@gmail.com
4 Department of Materials Science and Engineering, Kumoh National Institute of Technology, Gumi 39177, Republic of Korea; sungjinan@kumoh.ac.kr
5 Purpose-Based Mobility Group, Korea Institute of Industrial Technology (KITECH), Gwangju 06211, Republic of Korea
6 Advanced Materials Research Center, Kumoh National Institute of Technology, Gumi 39177, Republic of Korea
* Correspondence: jerwual@kitech.re.kr (J.-C.P.); drmspreddy@kumoh.ac.kr (S.P.R.M.)

Abstract: To realize highly sensitive SAW devices, novel Al–Cu thin films were developed using a combinatorial sputtering system. The Al–Cu sample library exhibited a wide range of chemical compositions and electrical resistivities, providing valuable insights for selecting optimal materials for SAW devices. Considering the significant influence of electrode resistivity and density on acoustic wave propagation, an Al–Cu film with 65 at% Al was selected as the IDT electrode material. The selected Al–Cu film demonstrated a resistivity of 6.0×10^{-5} Ω-cm and a density of 4.4 g/cm^3, making it suitable for SAW-based microfluidic actuator applications. XRD analysis revealed that the Al–Cu film consisted of a physical mixture of Al and Cu without the formation of Al–Cu alloy phases. The film exhibited a fine-grained microstructure with an average crystallite size of 7.5 nm and surface roughness of approximately 6 nm. The SAW device fabricated with Al–Cu IDT electrodes exhibited excellent acoustic performance, resonating at 143 MHz without frequency shift and achieving an insertion loss of −13.68 dB and a FWHM of 0.41 dB. In contrast, the Au electrode-based SAW device showed significantly degraded acoustic characteristics. Moreover, the SAW-based microfluidic module equipped with optimized Al–Cu IDT electrodes successfully separated 5 µm polystyrene (PS) particles even at high flow rates, outperforming devices with Au IDT electrodes. This enhanced performance can be attributed to the improved resonance characteristics of the SAW device, which resulted in a stronger acoustic radiation force exerted on the PS particles.

Keywords: surface acoustic wave; interdigital transducer; RF sputtering; aluminum–copper thin film

check for updates

Citation: Kim, H.; Lee, Y.; Puneetha, P.; An, S.J.; Park, J.-C.; Mallem, S.P.R. High-Performance SAW-Based Microfluidic Actuators Composed of Sputtered Al–Cu IDT Electrodes. *Coatings* **2024**, *14*, 1420. https://doi.org/10.3390/coatings14111420

Academic Editor: Andrei Ionut Mardare

Received: 30 September 2024
Revised: 5 November 2024
Accepted: 5 November 2024
Published: 8 November 2024

1. Introduction

Surface acoustic waves (SAWs) are elastic waves that travel along the surface of a piezoelectric material and were first discovered by Rayleigh in 1885 [1]. White and Voltmer subsequently elucidated the propagation phenomenon of SAWs, leading to the development of the interdigital transducer (IDT) in 1965 [2]. An IDT consists of two interdigitated comb-shaped metal electrodes deposited on a piezoelectric substrate. When a sinusoidal voltage is applied to the IDT, the piezoelectric effect induces mechanical vibrations in the substrate, generating acoustic waves that propagate perpendicularly to the IDT [3–6]. SAW technology has found widespread application in various fields, including wireless communication [7,8], mesoscopic systems [9,10], and sensing applications such as chemical vapor [11], humidity [12], biological [13,14], gas [15], pressure [16], and contaminant detection [17].

Microfluidic devices have gained significant attention in the biosensor field due to their ability to precisely manipulate minuscule volumes of samples and reagents. Such devices offer exceptional platforms for high-resolution and sensitive detection through processes such as separation and mixing [18]. Recently, the integration of various technologies, including electrowetting, magnetics, and optics, has significantly advanced the capabilities of microfluidic systems, particularly in SAW technology [19–21].

In a typical SAW sensor, a pair of IDTs are deposited on a piezoelectric substrate. One IDT serves as the input transducer, while the other acts as the output transducer. When an electrical signal is applied to the input IDT, it generates acoustic waves that propagate along the surface of the piezoelectric material. These waves, upon reaching the output IDT, induce an electrical signal due to the inverse piezoelectric effect. The phase shift and amplitude difference between the input and output signals are used to characterize the change in SAW velocity [22]. Traditionally, SAW sensors have employed single-metal electrodes, such as gold (Au) or aluminum (Al), on a lithium niobate ($LiNbO_3$) piezoelectric substrate. While Au electrodes offer excellent electrical properties, their high density can hinder the generation of high-frequency acoustic waves. Conversely, Al electrodes, though lightweight, exhibit relatively poor electrical conductivity, leading to increased device resistance. To overcome these limitations, there is a growing interest in developing composite materials that combine the advantages of both metals, resulting in improved SAW device performance.

Typically, SAW-IDT electrodes are fabricated using either electron beam evaporation or DC/RF sputtering. E-beam evaporation is ideal for depositing single-element films with high melting points. While multi-component alloys can be deposited using e-beam sources, the potential for phase changes can introduce defects in the film. In contrast, DC/RF sputtering offers greater flexibility, allowing for the deposition of thin films from various metals or non-metallic materials at lower temperatures. This makes it particularly suitable for fabricating composite thin films with diverse physical properties. Combinatorial sputtering, a variant of this technique, enables the rapid synthesis of thin films with compositional and thickness gradients, facilitating the efficient exploration of optimal material combinations [23,24].

This study investigates methods for significantly enhancing the performance of SAW-based microfluidic actuators by characterizing the physical and chemical properties of IDT electrodes, a critical component of SAW devices. Traditionally, IDT electrodes in SAW devices have been fabricated using single metals such as Al or Au. However, research on the multifunctional materials required for high-frequency resonance has been limited. Given their lightweight and high conductivity, Al–Cu thin films were identified as promising candidates for SAW devices and were systematically studied using combinatorial sputtering. By comprehensively analyzing the structural, chemical, and electrical properties of Al–Cu thin films through combinatorial sputtering, the optimal growth conditions for uniform films were established. The fabricated Al–Cu-based IDT electrodes were then integrated into SAW devices, and their impact on acoustic properties, such as resonant frequency and insertion loss, was compared with that of devices using Au electrodes. Additionally, the superior microparticle separation efficiency of SAW-based microfluidic actuators equipped with Al–Cu electrodes was verified.

2. Materials and Methods

Al–Cu thin films with different chemical, structural, and electrical properties were grown on 4-inch silicon substrates by combinatorial RF sputtering (ULVAC MB07-4501), and their application to SAW-IDT electrodes was systematically investigated. To obtain the Al–Cu thin films, single-metal Al and Cu targets were used, and the Al–Cu thin film was grown in a fixed state without rotation of the substrate to obtain the composition gradient.

The sputtering conditions for the compositionally graded Al–Cu thin films were as follows: RF power of 100 W (Al and Cu), base pressure of 3×10^{-6} Pa, working pressure of 0.21 Pa, flow gas, Ar (99.99%), and substrate temperature at room temperature. The Al–Cu thin films were cut into 6 pieces, and the structural/chemical/electrical properties of each sample were evaluated. The growth conditions for uniform Al content were as follows: RF power of 300 W (Al)/100 W (Cu), base pressure of 3×10^{-6} Pa, working pressure of 0.21 Pa, flow gas, Ar (99.99%), and substrate temperature at room temperature. To confirm the chemical/electrical uniformity of the Al–Cu films grown on 4-inch Si wafers, the changes in composition and resistivity characteristics of five Al–Cu samples taken from the wafer were closely analyzed. To achieve a resonant frequency of 143 MHz, a straight-type SAW-IDT pattern was designed. This pattern utilized 150 nm thick Al–Cu electrodes with a pattern width of 7 μm and a total IDT length of 2500 μm, comprising 90 electrode pairs. The IDT electrodes were fabricated on a 4-inch diameter $LiNbO_3$ substrate with a 128° Y-cut orientation. Prior to electrode deposition, the $LiNbO_3$ wafer underwent a thorough cleaning process using Piranha solution. Subsequently, the IDT patterns were defined through photolithography using a positive photoresist (AZ GXR 601). Two IDT patterns with Al–Cu and Au thin films were deposited by RF magnetron sputtering and E-beam evaporation, respectively. In addition, the structure of the IDT electrode with the Au film grown by the e-beam process completely matched the Al–Cu film growth conditions in terms of film thickness, pattern width, and electrode pairs. The acoustic properties of the SAW device composed of two types of IDT electrodes were investigated to determine their effect on the separation performance of PS particles in microfluidics. The acoustic radiation force was analyzed with the PS suspension, which had a concentration of 100 μg/L using spherical PS powder with 5 μm diameter dispersed in DI water. The PDMS microfluidic channel for PS microparticle separation consisted of one inlet port and two outlet ports, and finally the SAW-based microfluidic actuator module was thermally bonded by pressing the PDMS channel to the O_2 plasma-treated SAW device surface.

The compositional distribution and morphological properties of the Al–Cu thin films were examined by field-emission scanning microscopy (FE-SEM, Quanta 200, FEI, Hillsboro, OR, USA). The surface roughness of the Al–Cu thin film was analyzed using an atomic force microscope (AFM, XE-200, Park Systems, Suwon-si, Republic of Korea). The crystalline structure of Al–Cu thin films was analyzed by X-ray diffraction (XRD, PANalytical X'pert MPD, Malvern, UK). The electrical resistivity was determined by the Hall effect measurement system using the Van der Pauw geometry (Model 7707, Lake Shore Cryotronics, Westerville, OH, USA) at a constant magnetic field of 4 kG. The IDT patterns were observed using a 3D laser optical microscope (Model OLS4100-SAA, OLYMPUS, Tokyo, Japan). The resonant frequency of the SAW device was analyzed by a vector network analyzer (Model E5080B, Keysight, Santa Rosa, CA, USA).

3. Results

This study aims to develop a novel, lightweight, and highly conductive physically mixed Al–Cu film to replace conventional gold (Au) electrodes in SAW-IDT devices operating at 143 MHz. By employing combinatorial sputtering, we can systematically investigate a wide range of Al–Cu compositions to identify the optimal candidates for high-performance SAW-IDT applications. The selected composition will be further optimized through controlled deposition parameters to achieve the desired electrical properties and mechanical stability. Ultimately, the developed physically mixed Al–Cu thin films will be integrated into SAW-IDT devices to enhance their performance in microfluidic applications, such as particle manipulation and sensing. By leveraging the unique properties of Al and Cu, we anticipate significant advancements in the field of SAW devices. Figure 1 illustrates the schematic diagram of combinatorial sputtering for physically mixed Al–Cu thin films with compositional gradients. By simultaneously depositing Al and Cu on distinct targets, we can generate films with varying compositions across the substrate. This technique allows for a comprehensive exploration of the Al–Cu system, enabling the identification of optimal compositions for specific applications. When deposited without substrate rotation, the physically mixed Al–Cu films exhibit compositional gradients due to variations in deposition rates across the substrate. In contrast, substrate rotation ensures uniform film thickness and composition, properties that can be further fine-tuned by adjusting the RF power.

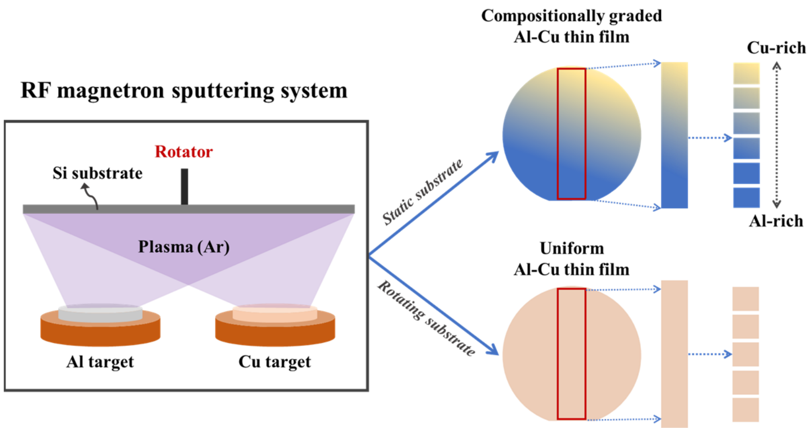

Figure 1. Schematic diagram of combinatorial sputtering to produce Al–Cu thin films with varying and uniform compositions.

Figure 2 shows thickness distribution and cross-section images of Al–Cu thin films as a function of sample position. It can be easily predicted that the AC1 sample grown near the Al target in the AC sample library would have high Al content, and the AC6 sample grown near the Cu target would have high Cu content. All the AC series films showed an average thickness distribution of 120 nm. As shown in Figure 2, the deposition rates of the Al-rich samples (AC1–AC3) are slightly higher than those of the Cu-rich films (AC4–AC6), which is due to the fast migration speed of the Al particles with relatively low density compared with the Cu particles under the same sputtering conditions. Additionally, the AC series samples showed remarkable adhesion properties without interface defects, as no voids or cracks were observed between the substrate and the thin film.

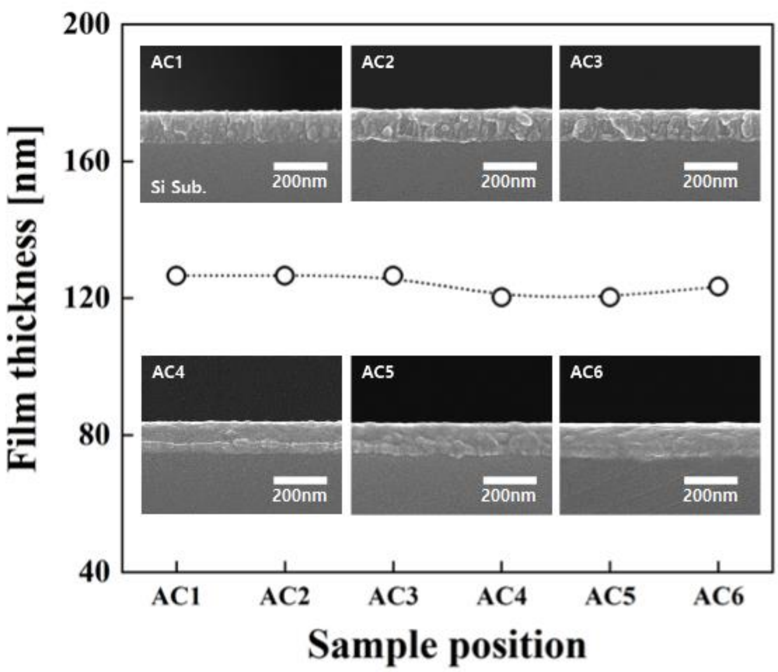

Figure 2. Thickness distribution and cross-section images of Al–Cu thin films [25].

Table 1 shows the chemical, electrical, and mechanical properties of Al–Cu thin films as a function of sample position. The Al and Cu contents of the AC samples linearly intersect as the AC sample number increases (the Al content decreases). The resistivity of the AC samples gradually decreases from 8.8 to 2.2 × 10^{-5} Ω-cm as the sample number increases, and the calculated density increases from 4.4 to 6.0 g/cm^3 as the sample number increases. The AC sample libraries grown by combinatorial sputtering have different compositions, resistivity, and density depending on the sample position, which can be used to derive factors that can improve the performance of the SAW device. In our previous study, it was demonstrated that IDT electrodes composed of AC thin films with high Al content can significantly improve the acoustic properties of SAW devices. For the SAW device with the resonant frequency of 70 MHz, it was verified that the insertion loss and the main frequency selectivity of the SAW device were improved when the Al content of the IDT electrode was ranged from 60 to 70 at%. Therefore, in this study, the IDT electrode for the resonant frequency of 143 MHz was fabricated using the AC thin film with an Al content of approximately 65 at%.

Table 1. Chemical composition, resistivity and calculated density of Al–Cu thin films as a function of sample position.

Sample		AC1	AC2	AC3	AC4	AC5	AC6
Composition (at%)	Al	64.9	57.6	53.4	48.3	45.7	38.4
	Cu	35.1	42.4	46.6	51.7	54.3	61.6
Resistivity (×10^{-5} Ω-cm)		8.9	7.3	5.0	3.4	2.6	2.2
Calculated density (g/cm^3)		4.4	4.9	5.1	5.4	5.6	6.0

To fabricate SAW-IDT electrodes, Al–Cu thin films with uniform thickness and composition were deposited on 4-inch Si substrates and closely investigated. Figure 3 presents the surface and cross-sectional SEM images of samples taken from different positions of the Al–Cu thin films grown on Si substrates. Samples S1, S2, and S3 represent the center, left, and right regions of the 4-inch wafer, respectively, to confirm the uniformity of the structural, chemical, electrical, and mechanical properties of the Al–Cu thin films.

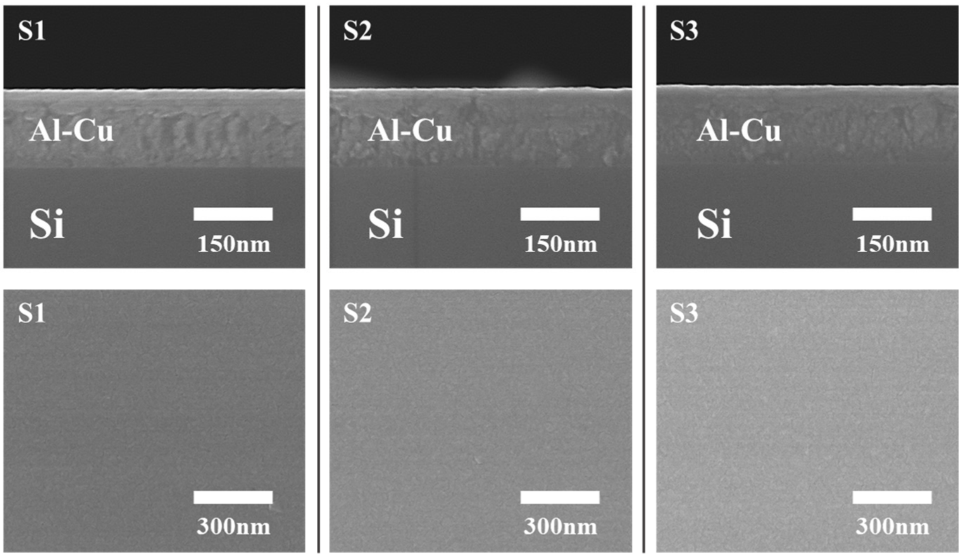

Figure 3. Surface and cross-sectional SEM images of Al–Cu thin films with uniform thickness and compositions.

As shown in Figure 3, the Al–Cu thin films grown by sputtering exhibited a uniform thickness of approximately 150 nm and stable interfacial adhesion without defects between the substrate and the film. Furthermore, no surface defects such as pinholes or cracks were observed on the surface of the Al–Cu thin films. Additionally, the chemical, electrical, and mechanical properties of the three Al–Cu thin film samples are summarized in Table 2. Regardless of the sample position, the Al–Cu thin films showed a nearly constant composition, with an Al content of 65 at%, indicating minimal compositional variation. The electrical resistivity also maintained a constant value of 6.0×10^{-6} ohm-cm on average. The density of the Al–Cu thin films was calculated as a composite density using the Al and Cu contents, and it showed the same value of 4.4 g/cm^3 due to the negligible compositional difference. The results of our investigation have unequivocally demonstrated that physically mixed Al–Cu thin films, with their uniform thickness and homogeneous aluminum content, offer a compelling solution for the development of lightweight and highly conductive SAW-IDT electrodes.

Table 2. Film thickness, composition, resistivity, and calculated density of Al–Cu thin films as a function of sample position.

Sample	S1	S2	S3
Film thickness (nm)	149.5 ± 1.3	150.3 ± 1.1	149.7 ± 1.5
Al content (at%)	64.5 ± 0.8	65.2 ± 0.5	64.8 ± 0.3
Resistivity (ohm-cm)	$5.8 \pm 0.2 \times 10^{-6}$	$6.2 \pm 0.1 \times 10^{-6}$	$6.1 \pm 0.3 \times 10^{-6}$
Calculated density (g/cm^3)	4.4	4.4	4.4

XRD analysis was conducted to elucidate the crystallinity of Al–Cu thin films grown via RF sputtering. Figure 4 presents the diffraction patterns of the Al–Cu thin films, denoted as S1, S2, and S3, revealing identical diffraction angles. The observed diffraction peaks at 38.49°, 42.38°, and 61.65° correspond with the (111), (200), and (220) planes of the face-centered cubic (FCC) Al structure, respectively. Similarly, the peaks at 38.49°, 44.01°, and 61.61° can be attributed to the (111), (200), and (220) planes of the FCC Cu structure. The overlapping of the (111) and (220) peaks from both Al and Cu suggests a physical mixture of individual Al and Cu crystals rather than a formed alloy, consistent with the suppression of alloy formation during film growth. This indicates the absence of defects caused by the formation of secondary phases within the Al–Cu thin films.

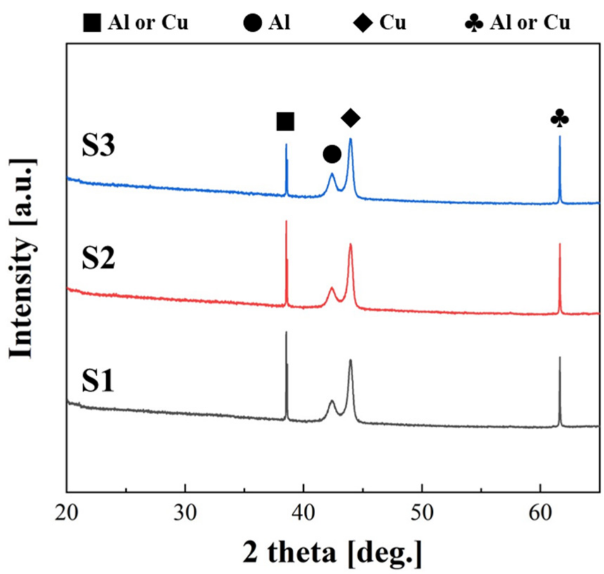

Figure 4. XRD patterns of Al–Cu thin films with uniform physical and chemical properties.

To further investigate the crystallographic behavior of the Al–Cu thin films, the full width at half maximum (FWHM) and crystallite size of the diffraction peaks from samples S1, S2, and S3 were calculated using the Scherrer equation and summarized in Table 3. The diffraction peaks from the uniform Al–Cu thin films exhibited nearly identical positions and FWHM values across all samples. Consequently, the average crystallite size was calculated to be approximately 7 nm for S1, S2, and S3, respectively. The consistently small crystallite size of around 7 nm in the Al–Cu thin films suggests a nanocrystalline structure. This fine-grained microstructure, obtained through RF sputtering at room temperature, can be attributed to several factors, including high nucleation rates, limited atomic mobility, and strain induced by the lattice mismatch between Al and Cu. The small crystallite size is thought to contribute to the enhanced mechanical properties and electrical conductivity of the Al–Cu thin films, making them promising candidates for various applications.

Table 3. Crystallite size and microstructure uniformity of Al–Cu thin films grown by combinatorial sputtering.

	2 theta [deg.]	FWHM [deg.]	Crystallite size [nm]
S1	38.49	0.12	12.5
	42.49	1.18	2.1
	43.94	0.49	4.8
	61.61	0.15	8.9
	Average		7.1
S2	2 theta [deg.]	FWHM [deg.]	Crystallite size [nm]
	38.51	0.11	13.5
	42.50	1.21	2
	43.95	0.48	5
	61.59	0.12	9.3
	Average		7.5
S3	2 theta [deg.]	FWHM [deg.]	Crystallite size [nm]
	38.50	0.11	13.6
	42.48	1.12	2
	43.93	0.51	4.7
	61.57	0.13	8.7
	Average		7.3

AFM analysis was employed to characterize the surface morphology of the Al–Cu thin films and revealed distinct surface features across the samples, as shown in Figure 5. Sample S1 exhibited the smoothest surface with an average roughness (Ra) of 1.14 nm, indicating a highly uniform and dense microstructure. In contrast, samples S2 and S3 showed progressively rougher surfaces, with Ra values of 6.90 nm and 9.86 nm, respectively. This variation in surface roughness correlates strongly with the results obtained from X-ray diffraction (XRD) analysis. The sample with the smallest crystallite size (S1) exhibited the smoothest surface, suggesting that a finer grain size contributes to more uniform and denser microstructure. Conversely, the larger crystallite sizes in samples S2 and S3 are associated with increased surface roughness, likely due to the formation of larger grains and grain boundaries.

While the variation in surface roughness across different regions of the wafer may indicate non-uniform growth conditions, it is important to note that this does not necessarily have a negative impact on the performance of SAW devices. While a smoother surface, as observed in sample S1, is generally advantageous for minimizing surface scattering and enhancing electrical conductivity, a slightly rougher surface can improve mechanical properties such as adhesion and wear resistance, which may be beneficial for device durability. The optimal surface roughness for SAW devices will depend on the specific application and the desired balance between electrical and mechanical performance.

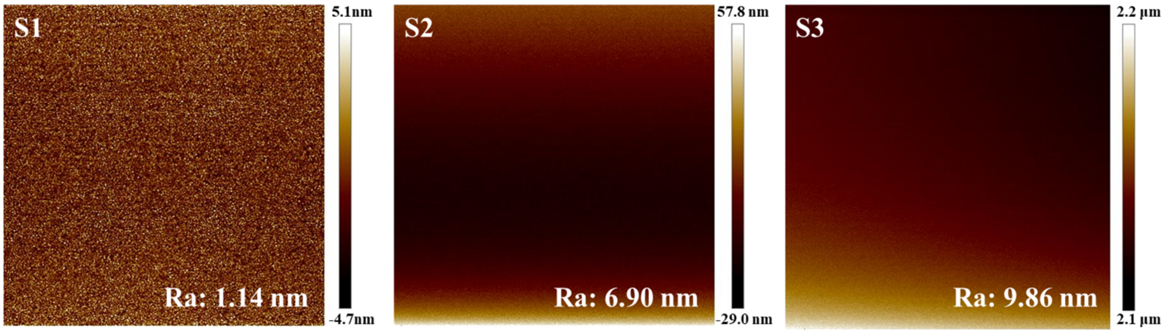

Figure 5. AFM topography images of sputter-deposited Al–Cu thin films (S1, S2, S3) with different surface roughness values.

To effectively manipulate 5 µm polystyrene (PS) particles in a microfluidic environment, it is crucial to satisfy the Mie scattering condition. This condition requires a specific relationship between the particle size and the wavelength of the acoustic wave, which is directly linked to the resonant frequency of the SAW device. For this reason, the resonant frequency for controlling 5 µm PS particles in microfluidics was calculated by the following equation [26]:

$$k = \pi f \, \mathrm{d}/\mathrm{c_f} \tag{1}$$

where k is the Helmholtz number, f is the resonant frequency and c_f is the speed of an acoustic wave in pure water. When the Helmholtz number (k) met the Mie scattering condition of 1.5, the resonant frequency required to control 5 µm polystyrene (PS) particles was confirmed to be 143 MHz. To obtain the resonant frequency suitable for separating 5 µm PS particles, the acoustic frequency was calculated using the following equation [26]:

$$f = \mathrm{c_s}/\lambda \tag{2}$$

where c_s is the speed of an acoustic wave in the piezoelectric substrate and λ is the wavelength of SAWs. The SAWs are directly influenced by the IDT configuration and can be quantitatively determined using the following equation [27]:

$$\lambda = 4\mathrm{d} \tag{3}$$

where λ is the wavelength of SAWs and d is the width of IDTs (assuming the width and the spatial distance of IDTs are the same). By employing mathematical modeling tools such as Mathematica, a comprehensive analysis of the relationships between various design parameters, including IDT pattern width, number of electrode pairs, film thickness, and total electrode length, was conducted to investigate their impact on the intensity and frequency of acoustic waves generated by the SAW device. Figure 6a presents the detailed results of the resonant frequency as a function of IDT pattern width. It was determined that a 7 µm pattern width was necessary to achieve the target resonant frequency of 143 MHz. Figure 6b illustrates the correlation between the number of electrode pairs and the total IDT length required to ensure impedance matching with a 50 Ω reference impedance. In this study, a configuration with 90 electrode pairs and a total IDT length of 2500 µm was selected to meet these specifications.

Figure 7 shows the resonant frequency of the SAW device fabricated with Al–Cu thin films with an Al content of 65 at%. In addition, the resonance frequency of the SAW device fabricated with Au-IDT electrodes are also depicted. Both devices had an identical pattern width of 7 µm, total IDT length of 2500 µm, film thickness of 150 nm, and 90 electrode pairs, and the acoustic characteristics of the SAW devices as a function of IDT electrode material were closely investigated. As shown in Figure 7, both SAW devices exhibited an identical resonant frequency of 143 MHz, confirming that they were normally fabricated without any defects in the designed IDT patterns. However, at the 143 MHz resonant frequency, there was a significant difference in insertion loss and peak selectivity between the two devices. The SAW device composed of Al–Cu electrodes exhibited an insertion loss of −13.68 dB and FWHM of 0.41 dB, whereas the SAW device composed of Au electrodes exhibited an insertion loss of −5.16 dB and FWHM of 1.0 dB. This difference can be explained by the fact that the vibration frequency generated from the piezoelectric substrate was determined by the mechanical properties related to the density rather than the electrical properties of the IDT electrodes. In other words, the electrical energy applied from the IDT electrodes was converted into mechanical energy that expanded or contracted the crystal of the piezoelectric material by the inverse piezoelectric effect. At this time, the density of the IDTs formed on the piezoelectric material can locally limit the generation of acoustic waves, thereby reducing the insertion loss and selectivity characteristics of the resonant frequency. From these results, it was demonstrated that the acoustic performance of the SAW device with the Al–Cu electrode, which has relatively low density and appropriate electrical characteristics, is superior to that of the device composed of the Au electrode.

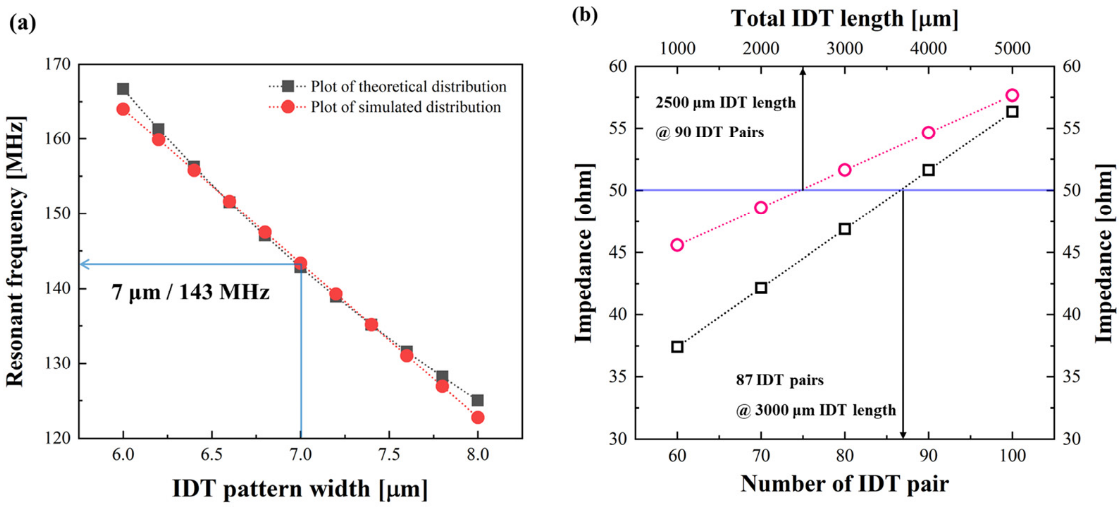

Figure 6. SAW-IDT pattern design for separating 5 μm PS micro-particles. (**a**) Distribution of resonant frequency depending on IDT pattern width and (**b**) relationship between total IDT length and electrode pairs at the reference impedance of 50 Ω.

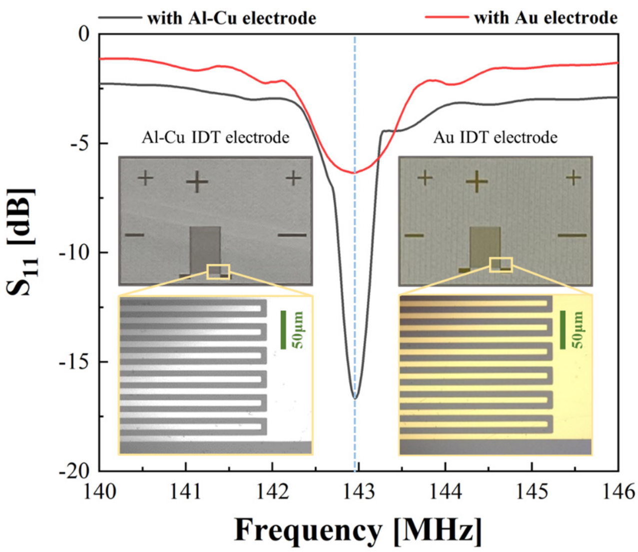

Figure 7. Resonant frequency of SAW devices with Al–Cu and Au electrode.

The surface acoustic wave (SAW)-based microfluidic actuator module was fabricated for efficient separation of 5 μm polystyrene (PS) particles, as shown in Figure 8a. The SAW module, comprising a PDMS microchannel, SAW device, and PCB, was designed to operate at a resonant frequency of 143 MHz, enabling precise control over PS particles. Figure 8b illustrates the separation efficiency of PS particles as a function of flow rate for the PS suspension with a concentration of 100 μg/L. The PS particle separation efficiency was calculated by the following simple equation:

$$\text{PS separation efficiency (\%)} = N_D \times 100/(N_D + N_O) \quad (4)$$

where N is the number of PS particles measured by optical microscope, D is the drain port at the PDMS microfluidic channel, O is the outlet port at the PDMS microfluidic channel.

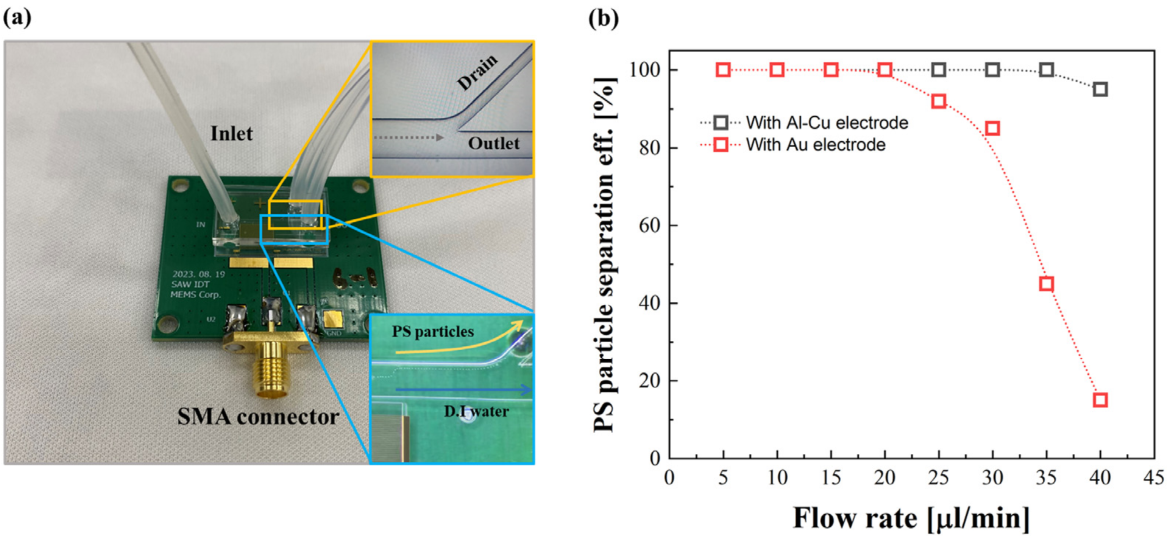

Figure 8. SAW-based microfluidic actuator module for 5 μm PS particle separation. (**a**) Picture of SAW-based microfluidic actuator module and (**b**) separation efficiency of PS particles according to the flow rate of PS suspension with a concentration of 100 μg/L.

Experimental results revealed that both the Al–Cu and Au electrode-based SAW modules achieved complete separation of PS particles at a flow rate below 20 μL/min. However, the separation efficiency of the Au electrode-based module decreased significantly at a flow rate exceeding 25 μL/min. In contrast, the Al–Cu interdigital transducer (IDT) electrode-based module maintained stable separation performance even at high flow rates. Figure 9's optical microscopy images provide additional evidence supporting the aforementioned results. At a flow rate of 25 μL/min, all PS particles in the Al–Cu IDT-based module migrated to the drain port, while some particles were observed at the outlet port in the Au electrode-based module. This indicates that the superior resonant characteristics of the Al–Cu IDT electrode enabled the generation of a stronger acoustic radiation force, overcoming fluidic resistance at high flow rates and facilitating efficient particle separation.

These results show that the acoustic radiation force required for particle manipulation in microfluidics is highly dependent on the resonant properties of the SAW-IDT, which, in turn, is determined by the material and structural characteristics of the IDT electrode. The Al–Cu-based SAW-IDT electrode employed in this study exhibited excellent electrical and mechanical properties, contributing to enhanced SAW device performance. The low resistivity, low electrode density, and stable crystalline structure of the Al–Cu alloy facilitated the generation of high-quality acoustic waves, resulting in improved particle separation efficiency.

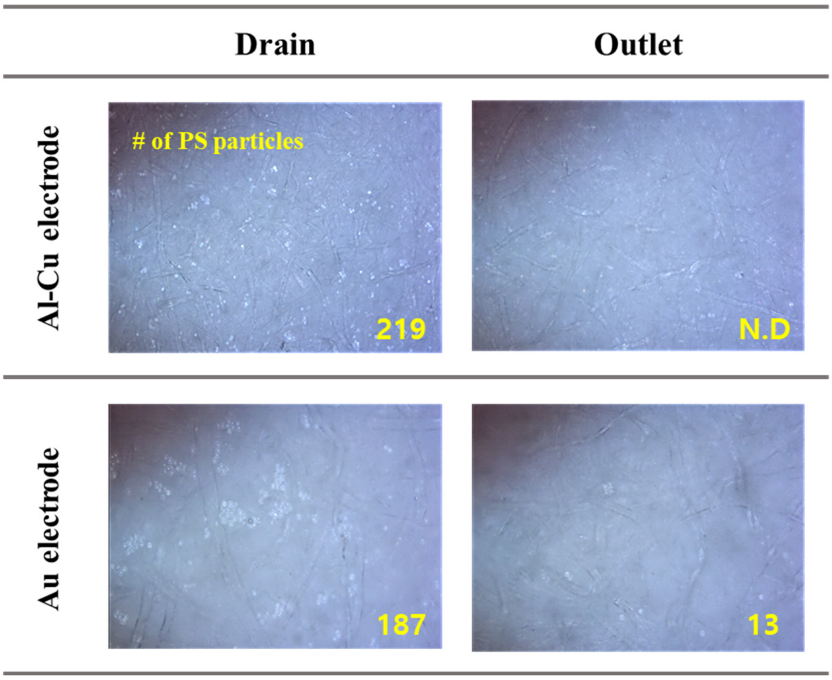

Figure 9. Optical microscope images of PS particles captured at the drain/outlet ports in the SAW actuator module consisting of two different electrodes.

Future studies will focus on optimizing the performance of SAW-IDT electrodes by systematically investigating the microstructural and electrical properties of Al–Cu thin films as a function of growth temperature. Specifically, the effects of growth temperature on the crystallite size, surface roughness, and formation of secondary phases in Al–Cu thin films will be examined to elucidate their impact on SAW device performance. This research is expected to lay the groundwork for the development of high-performance SAW devices.

4. Conclusions

The Al–Cu thin films with compositional gradients were deposited simultaneously by using a combinatorial sputtering system for selecting candidate materials for IDT electrodes used in SAW devices. The Al–Cu sample libraries showed the various chemical compositions and electrical resistivity as a function of sample position. From these, the Al–Cu thin film with an Al content of 65 at% was selected as the IDT material of the SAW-based microfluidic actuator, as its electrical resistivity and density were the most suitable for generating acoustic waves from the piezoelectric materials. The Al–Cu IDT for generating 143 MHz resonance frequency was designed and fabricated with a pattern width of 7 µm, a film thickness of 150 nm, and 90 electrode pairs. The SAW device fabricated with an Al–Cu electrode on $LiNbO_3$ substrate showed significantly improved acoustic performance, with an insertion loss of −13.68 dB and a main peak selectivity of 0.41 dB compared with the commercial Au electrode. The SAW-based microfluidic module composed of Al–Cu IDT electrodes with an Al content of 65 at% completely separated 5 µm PS particles in the flow rate range of 5 to 35 µL/min, but the SAW module composed of the Au IDT electrode showed a sharp decrease in PS separation efficiency at a flow rate of 20 µL/min. From the perspective of particle control in microfluidics based on SAW technology, it has been demonstrated that the performance of the entire SAW system can be dramatically improved when the electrical conductivity and low-density characteristics of the IDT electrode, which are key components that determine the performance of the SAW device, are simultaneously satisfied. Future studies will aim to optimize the performance of Al–Cu-based SAW-IDTs by investigating the properties of thin films grown under conditions that suppress alloy phase formation. Specifically, the relationship between growth temperature, film characteristics, and the acoustic and microparticle control properties of SAW devices will be explored.

Author Contributions: Conceptualization, H.K. and J.-C.P.; methodology, H.K. and J.-C.P.; validation, H.K., Y.L., P.P., S.J.A. and J.-C.P.; formal analysis, H.K., Y.L., P.P., S.J.A., J.-C.P. and S.P.R.M.; investigation, H.K., Y.L., J.-C.P. and S.P.R.M.; resources, J.-C.P. and S.P.R.M.; writing—original draft preparation H.K., Y.L. and J.-C.P.; writing—review and editing, H.K., J.-C.P. and S.P.R.M.; visualization, Y.L., P.P. and S.J.A.; supervision, J.-C.P. and S.P.R.M. All authors have read and agreed to the published version of the manuscript.

Funding: This study has been conducted with the support of Korea Industrial Complex Corporation as "Competitiveness reinforcement project for industrial clusters (1415189052)" and the Korea Institute of Industrial Technology as "Development of Core Technologies for a Smart Mobility (KITECH JA-24-0001)". The NRF grants (2018R1A6A1A03025761) were funded by the Korean government. The Korea Innovation Foundation ((INNOPOLIS) grant MSIT) (2020-DD-UP-0278) was funded by the Korean Government.

Institutional Review Board Statement: Not applicable.

Informed Consent Statement: Not applicable.

Data Availability Statement: The data are available upon reasonable request from the corresponding author.

Conflicts of Interest: Author Hwansun Kim was employed by the company Micro Electro Mechanical System (MEMS) Corp. The remaining authors declare that the research was conducted in the absence of any commercial or financial relationships that could be construed as a potential conflict of interest.

References

1. Rayleigh, L. On waves propagated along the plane surface of an elastic solid. *Proc. London Math. Soc.* **1885**, *1*, 4–11. [CrossRef]
2. White, R.M.; Voltmer, F.W. Direct piezoelectric coupling to surface elastic waves. *Appl. Phys. Lett.* **1965**, *7*, 314–316. [CrossRef]
3. Jiang, Z.; Liu, B.; Hao, Y. Research progresses in preparation methods and applications of zinc oxide nanoparticles. *J. Alloys Compd.* **2023**, *956*, 170316. [CrossRef]
4. Augustine, R.; Sarry, F.; Kalarikkal, N.; Thomas, S.; Badie, L.; Rouxel, D. Surface acoustic wave device with reduced insertion loss by electrospinning p(VDF–TRFE)/ZnO nanocomposites. *Nanomicro Lett.* **2016**, *8*, 282–290. [CrossRef]
5. Phan, D.-T.; Chung, G.-S. Surface acoustic wave hydrogen sensors based on ZnO nanoparticles incorporated with a Pt catalyst. *Sens. Actuators B Chem.* **2012**, *161*, 341–348. [CrossRef]
6. Guo, Y.; Zhao, C.; Zhou, X.; Li, Y.; Zu, X.-T.; Gibson, D.; Fu, Y.Q. Ultraviolet sensing based on nanostructured ZnO/Si surface acoustic wave devices. *Smart Mater. Struct.* **2015**, *24*, 125015. [CrossRef]
7. Campbell, C. *Surface Acoustic Wave Devices for Mobile and Wireless Communications, Four-Volume Set*; Academic Press: Cambridge, MA, USA, 1998.
8. Shao, L.; Zhu, D.; Colangelo, M.; Lee, D.; Sinclair, N.; Hu, Y.; Rakich, P.T.; Lai, K.; Berggren, K.K.; Loncar, M. Electrical control of surface acoustic waves. *Nat. Electron.* **2022**, *5*, 348–355. [CrossRef]
9. Peri, V.; Song, Z.-D.; Serra-Garcia, M.; Engeler, P.; Queiroz, R.; Huang, X.; Deng, W.; Liu, Z.; Bernevig, B.A.; Huber, S.D. Experimental characterization of fragile topology in an acoustic metamaterial. *Science* **2020**, *367*, 797–800. [CrossRef]
10. Okada, A.; Oguro, F.; Noguchi, A.; Tabuchi, Y.; Yamazaki, R.; Usami, K.; Nakamura, Y. Cavity enhancement of anti- stokes scattering via optomechanical coupling with surface acoustic waves. *Phys. Rev. Appl.* **2018**, *10*, 024002. [CrossRef]
11. Liu, S.; Sun, H.; Nagarajan, R.; Kumar, J.; Gu, Z.; Cho, J.; Kurup, P. Dynamic chemical vapor sensing with nanofibrous film based surface acoustic wave sensors. *Sens. Actuators A* **2011**, *167*, 8–13. [CrossRef]
12. Hallil, H.; Zhang, Q.; Flahaut, E.; Lachaud, J.-L.; Coquet, P.; Dejous, C.; Rebiere, D. Guided SH-SAW sensor based on DWNTs sensitive material for VOCs and humidity detection. *J. Integr. Circuits Syst.* **2018**, *13*, 1–4. [CrossRef]
13. Ji, J.; Yang, C.; Zhang, F.; Shang, Z.; Xu, Y.; Chen, Y.; Chen, M.; Mu, X. A high sensitive SH-SAW biosensor based 36 YX black $LiTaO_3$ for label-free detection of Pseudomonas Aeruginosa. *Sens. Actuators B* **2019**, *281*, 757–764. [CrossRef]
14. Li, H.-Y.; Jia, W.-N.; Li, X.-Y.; Zhang, L.; Liu, C.; Wu, J. Advances in detection of infectious agents by aptamer- based technologies. *Emerg. Microbes Infect.* **2020**, *9*, 1671–1681. [CrossRef]
15. Jahanshahi, P.; Wei, Q.; Jie, Z.; Zalnezhad, E. Designing a non-invasive surface acoustic resonator for ultra-high sensitive ethanol detection for an on-the-spot health monitoring system. *Biotechnol. Bioprocess Eng.* **2018**, *23*, 394–404. [CrossRef]
16. Li, Y.; Li, J.; Huang, J.; Zhou, H. Fitting analysis and research of measured data of SAW micro-pressure sensor based on BP neural network. *Measurement* **2020**, *155*, 107533. [CrossRef]
17. Ho, C.K.; Lindgren, E.R.; Rawlinson, K.S. Development of a Surface Acoustic Wave Sensor for In-Situ Monitoring of Volatile Organic Compounds. *Sensors* **2003**, *3*, 236–247. [CrossRef]
18. Whitesides, G.M. The origins and the future of microfluidics. *Nature* **2006**, *442*, 368–373. [CrossRef]
19. Teng, P.; Tian, D.; Fu, H.; Wang, S. Recent progress of electrowetting for droplet manipulation: From wetting to superwetting systems. *Mater. Chem. Front.* **2020**, *4*, 140–154. [CrossRef]

20. Chen, G.; Ji, B.; Gao, Y.; Wang, C.; Wu, J.; Zhou, B.; Wen, W. Towards the rapid and efficient mixing on 'open- surface' droplet-based microfluidics via magnetic actuation. *Sens. Actuators B* **2019**, *286*, 181–190. [CrossRef]
21. Yang, H.; Gijs, M.A. Micro-optics for microfluidic analytical applications. *Chem. Soc. Rev.* **2018**, *47*, 1391–1458. [CrossRef]
22. Arruda, D.L.; Wilson, W.C.; Nguyen, C.; Yao, Q.W.; Caiazzo, R.J.; Talpasanu, I.; Dow, D.E.; Liu, B.C. Microelectrical sensors as emerging platforms for protein biomarker detection in point-of-care diagnostics. *Expert Rev. Mol. Diagn.* **2009**, *9*, 749–755. [CrossRef] [PubMed]
23. Park, J.-C.; Kim, T.-W. Bandgap engineering of $Cu(In_{1-x}Ga_x)Se_2$ absorber layers fabricated using $CuInSe_2$ and $CuGaSe_2$ targets for one-step sputtering process. *Opt. Mater. Express* **2016**, *6*, 3541. [CrossRef]
24. Nagy, P.; Gubicza, J. Mapping the microstructure and the mechanical performance of a combinatorial Co–Cr–Cu–Fe–Ni–Zn high-entropy alloy thin film processed by magnetron sputtering technique. *J. Mater. Res. Technol.* **2024**, *31*, 47–61. [CrossRef]
25. Eom, J.; Park, J.-C.; Mallem, S.P.R. Growth of Al–Cu Thin Films on $LiNbO_3$ Substrates for Surface Acoustic Wave Devices Based on Combinatorial Radio Frequency Magnetron Sputtering. *Crystals* **2024**, *14*, 844. [CrossRef]
26. Chanaud, R.C. Effects of geometry on the resonance frequency of Helmholtz resonators. *J. Sound Vib.* **1994**, *178*, 337–348. [CrossRef]
27. Cheeke, J. *Fundamentals and Applications of Ultrasonic Waves*; CRC Press: Boca Raton, FL, USA, 2010.